Local hydraulic resistance in heterogeneous porous media

Quirine Krol[1], Itzhak Fouxon[2], Pascal Corso[1], and Markus Holzner[1]

[1]ETHZ
[2]Yonsei University

November 23, 2022

Abstract

We examine the validity of the commonly used Hagen-Poiseuille model of local resistance of porous media using direct numerical simulations. We provide theoretical arguments that highlight possible limitations of this model and formulate a new constitutive model that is based on the circularity of iso-pressure surfaces. We compare the performance of both models on three different three-dimensional artificial porous media. We show that the new model improves the root-mean-squared-relative error from 59 %, 48 % and 32 % for the HP model to 12 % ,14 % and 18 % for the three porous media respectively. We anticipate that our approach may find broad application in network models of porous media that are typically build from 3D images with intricate pore geometries.

Local hydraulic resistance in heterogeneous porous media

Quirine Krol[1], **Itzhak Fouxon** [1,2], **Pascal Corso** [1], **Markus Holzner** [1,3,4]

[1]ETH Zurich, Stefano Franscini-Platz 5, 8093 Zurich, Switzerland
[2]Department of Computational Science and Engineering, Yonsei University, Seoul 120-749, South Korea
[3]Swiss Federal Institute for Water Science and Technology EAWAG
[4]Swiss Federal Institute for Forest, Snow and Landscape Research WSL

Corresponding author: Quirine Krol, `quirine.krol@protonmail.com`

Abstract

We examine the validity of the commonly used Hagen-Poiseuille model of local resistance of porous media using direct numerical simulations. We provide theoretical arguments that highlight possible limitations of this model and formulate a new constitutive model that is based on the circularity of iso-pressure surfaces. We compare the performance of both models on three different three-dimensional artificial porous media. We show that the new model improves the root-mean-squared-relative error from 59%, 48% and 32% for the HP model to 12%, 14% and 18% for the three porous media respectively. We anticipate that our approach may find broad application in network models of porous media that are typically build from 3D images with intricate pore geometries.

1 Introduction

Porous media flow is important for a wide range of applications in nature and technology, spanning from groundwater remediation and oil recovery to packed bed reactors and particle filters. In these flows, the highly complex and three-dimensional pore geometries give rise to complicated pore velocity fields that form the backbone for transport, mixing and chemical reaction processes. Detailed knowledge of these velocity fields is important for the modelling of effective parameters, most notably the permeability and the prediction of transport in porous media (Bear, 1972; Scheidegger, 1974). Despite its importance and extensive research, however, the relation between geometrical features of porous media and the resulting flow is still not fully understood.

Given that detailed knowledge of geometrical features of porous media is often unavailable, the classical flow modeling approach has been to represent the porous medium as a lattice of circular tubes that represent the pore network (Scheidegger, 1974). The flow in the tubes is assumed uniform and the velocity profile parabolic. While this is a rather crude approximation of the real geometry and flow behaviors, it has provided useful predictions for flow and transport. Early studies have modelled velocity distributions (Haring & Greenkorn, 1970), permeability (Fatt, 1956; Katz & Thompson, 1986) and particle dispersion (Saffman, 1959) based on bulk statistics of the medium geometry such as pore size distributions. These early studies have spurred many subsequent works on statistical pore scale models e.g. Dullien (1975); Kutsovsky et al. (1996); Maier et al. (1999); de Anna et al. (2017) and Dentz et al. (2018). The second class of models that hinges on the simplified lattice representation of porous media are the so-called pore network models (Thompson & Fogler, 1997). For both classes of models, the simplified modelling of local hydraulic resistance of individual pores based on Hagen-Poiseuille is a central element.

Many authors tried to relate the statistics of pore velocity to statistics of pore geometry represented by e.g. the local pore radius and the connectivity between pores. For example, one of the simplest models is the so-called *capillary bundle* model, in which the porous medium is conceptualized as a parallel arrangement of capillaries with given pore sizes (Scheidegger, 1974). Extensions of this model include parallel arrangements of wavy tubes (Le Borgne et al., 2011). These simple models are not appropriate for complex porous media, for which the network aspect is important. That is, in general, the connectivity between pores cannot be neglected and the concept of the linear pore breaks down (Dentz et al., 2018). An ad-hoc model that conceptualizes flow in porous media as a system of serial and parallel pore arrangements can be found in Holzner et al. (2015), and the resulting dispersion of tracers was predicted by Fouxon and Holzner (2016). Siena et al. (2014) and Hyman et al. (2012) statistically related velocity distributions to pore size distributions of statistically generated 3D porous media. Based on direct numerical simulations in 2D porous media composed of disks, de Anna et al. (2017) showed that the low velocity tail of the pore velocity distribution is governed by local pore size. This is a notable result as it suggests that the slow flow velocities are not strongly dependent on the connectivity between pores. Alim et al. (2017) showed that pore velocity distributions are governed by local correlations of pore sizes that organize flux ratios at pore junctions, while pore size itself was a poor predictor of flux ratios. They simplified two-dimensional porous medium flow by a network of tubes with varying diameter and the flow within each tube was calculated by solving for Kirchoffs circuit law for two-dimensional Poiseuille flow within the tubes of rectangular cross section. Even though using tubes with varying diameter is a refinement compared to simpler models with tubes of constant diameter, the simplification with respect to real geometries is still strong. Despite this, a comparison of simulation results with the experimentally obtained velocity distribution in a two-dimensional micromodel composed of pillars showed reasonable agreement (Alim et al., 2017). As mentioned, the statistical models in these works are based on the concept that local velocity profiles are parabolic. Some recent papers provided qualitative examples comparing pore velocity profiles to a parabola that suggest the assumption may be reasonable (de Anna et al., 2017; Dentz et al., 2018) and some evidence is provided by the comparison between simulations and experiments by Alim et al. (2017). However, a rigorous assessment of local hydraulic resistance in three-dimensional pore geometries is still missing in the literature.

With the advent of experimental techniques like micro-computed tomography there is now access to impressive details of three dimensional porous media architectures. Even though today's computing facilities make it possible to solve flow and transport with unprecedented accuracy in these complex geometries using direct numerical simulations, this approach is only feasible in small domains. Simple models that reduce the full complexity of real porous media are still needed. A lattice representation is the standard approach in so-called pore network models in which a Kirchhoff-type system of equations is solved to model single or multiphase porous medium flows (Thompson & Fogler, 1997) especially in absence of a detailed microstructure. The lattice is usually constructed based on data from experimental pore scale characterization measurements, e.g. imaging or mercury intrusion porosimetry. These pore network models are a valuable tool for understanding meso-scale phenomena, linking single pore processes and continuum porous media used in engineering (Xiong et al., 2016). Besides a sound network construction approach that mimics the real media, another critical aspect for the accuracy of modeling is the representation of local hydraulic resistance in the pores.

In this paper we start with a theoretical background where we define local pores based on consecutive iso-pressure surfaces, followed by a new model for the local hydraulic conductivity. In the methods section we describe our numerical experiment consisting of direct numerical simulations (DNS) from which we obtain local velocity and pressure data in heterogeneous porous media. Based on a post-processing of the DNS data we can extract the local hydraulic conductivity of a local pore. In the results we compare the measured hydraulic resistances to the Hagen-Poiseuille model and to the newly formulated model based a local shape parameter circularity. In the discussion we treat the limitations and extrapolations of the newly proposed model. In the final chapter we provide our conclusions.

2 Theoretical Background

For low Reynolds numbers and incompressible flow, the local flow in a porous media is described by the Stokes equations,

$$\nabla p = \mu \nabla^2 \mathbf{u}\,, \quad \nabla \cdot \mathbf{u} = 0 \tag{1}$$

with pressure p and velocity $\mathbf{u}$ and dynamic viscosity μ. For an arbitrary volume $\mathcal{V}$ in a porous media, enclosed by surface $\partial\mathcal{V}$ given by two iso-pressure surfaces $\mathcal{S}_{p_1}$ and $\mathcal{S}_{p_2}$ and solid-liquid surface boundary Γ, we can write down the integral form of the Stokes equations using the divergence theorem.

$$\int_{\mathcal{V}} \left(\mathbf{u}\cdot\nabla p - \mu\mathbf{u}\cdot\nabla^2\mathbf{u}\right) dV = \int_{\partial\mathcal{V}} p\,\mathbf{u}\cdot\mathbf{n}\,dS - \mu\int_{\partial\mathcal{V}} \mathbf{u}\cdot(\nabla\otimes\mathbf{u})\mathbf{n}\,dS + \mu\int_{\mathcal{V}}(\nabla\otimes\mathbf{u})^2 dV = 0, \tag{2}$$

with $\mathbf{n}$ the normal vector pointing outwards of surface ∂V, and $\otimes$ the dyadic product. Given that at the porous media boundary domain Γ we have a no-slip condition $\mathbf{u} = 0$ we can write

$$Q\Delta p = -\mu \int_{S_{p_1}+S_{p_2}} \mathbf{u}\cdot(\nabla\otimes\mathbf{u})\mathbf{n}\,dS + \mu\int_{\mathcal{V}}(\nabla\otimes\mathbf{u})^2 dV, \tag{3}$$

with the total flux through any cross section defined by

$$Q = \int \mathbf{u}\cdot\mathbf{n}\,dS. \tag{4}$$

Here we introduce the notion of disconnected iso-pressure surface $\mathcal{S}_i(p)$ for a given pressure value p. Iso-pressure surfaces are usually disconnected because they exist in the fluid domain only and are thus interrupted by the solid phase of the media. The first term of Eq. (2), the boundary term, will be less significant when the total volume V is enlarged by increasing δp. Furthermore, when we have saturated conditions, the complete pore space can be compartmentalized in a network of enclosed volumes $V_i(p_i, p_i{+}\delta p_i)$, which we will later call pores. We have assessed the relevance of the boundary term to $Q\Delta p$ for ten pores in the SI. We found that they contribute generally below 5% for the shortest available pores to below 1% for average size pores. Therefore it is reasonable to estimate Eq. (2) by

$$Q\Delta p \approx \mu\int(\nabla\otimes\mathbf{u})^2 dV. \tag{5}$$

In the following we apply a decomposition of the velocity vector $\mathbf{u} = u_p\hat{\mathbf{p}} + u_r\hat{\mathbf{r}}$ with $\hat{\mathbf{p}} = \nabla p/|\nabla p|$ (longitudinal direction in respect to the flow) and $\hat{\mathbf{p}}$ perpendicular to $\hat{\mathbf{r}}$ (transversal direction in respect to the flow). We assume that the most important

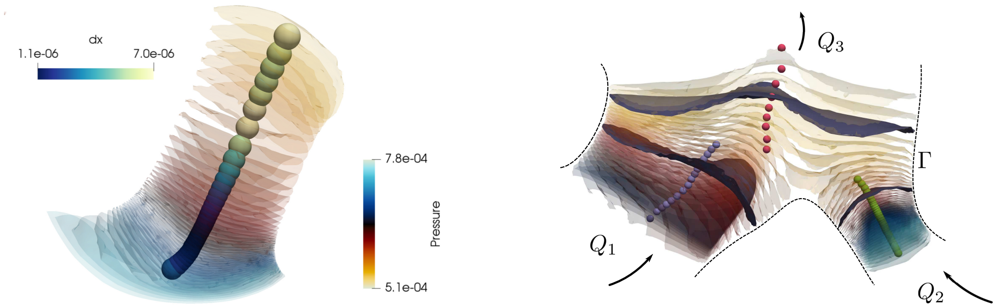

Figure 1: Left: A visualization of a collection of consecutive iso-pressure surfaces comprising one pore, including the center of mass of the iso-pressure surfaces indicated by the spheres. The color code of the spheres is given by the distance between the average coordinates between two consecutive iso-pressure surfaces. Right: A visualization of a junction of three pores for which the total flux is conserved $Q_1 + Q_2 = Q_3$. This visualization is based on a subset of the DNS results of porous media #2

contributions to the viscous dissipation tensor $\nabla_i u_j$ are given by $\nabla_i u_p$ i.e. $\nabla_i u_r \ll \nabla_i u_p$. Also this assumption has been verified in the supplementary information (SI) for the porous media that we have used below and leads to

$$|\nabla_i u_j|^2 \approx |\nabla_r u_p|^2 + |\nabla_p u_p|^2 . \tag{6}$$

Here the first term is expected to be more important for gradually varying pore geometries since gradients in the velocity in the longitudinal direction are usually much lower than in transverse direction. Equations (1)-(6) are valid for arbitrary volumes V. When we consider viscous dissipation in an *infinitesimal* volume dV enclosed by $\mathcal{S}(p), \mathcal{S}(p+\delta p)$ (with respective areas $A(p), A(p+\delta p)$), separated by average distance dx defined by $dV = A(p)dx$, we can estimate (analogous to Mortensen et al. (2005)) the average value of the first term of Eq. (6) by

$$|\nabla_r u_p|^2 = 8\pi \left(\alpha_0 + \alpha_1 \mathcal{C}\right) \frac{Q^2}{A^3} \quad , \tag{7}$$

with circularity parameter $\mathcal{C} = \mathcal{L}^2/4\pi A(p)$ with perimeter $\mathcal{L} = \int_{\partial\mathcal{S}(p)} dl$. The circularity parameter is related to the compactness factor $C = \mathcal{C}/4\pi$ in (Mortensen et al., 2005), and for HP flow it is equal to one. The coefficients α_0 and α_1 can be calculated (in first order of circularity) analytically or numerically for simple shapes of the iso-pressure surfaces, such as squares, triangles, or a perturbation of a sphere by spherical harmonics (Mortensen et al., 2005). For heterogeneous media the class of shapes are generally unknown and not symmetric, and therefore α_0 and α_1 are expected to be intrinsically dependent on the pore geometry and therefore to change from pore to pore.

For the second, longitudinal term, we can assume that the total flux Q remains constant for $p \to p{+}dp$, and the change of the velocity in longitudinal direction is caused by a change in cross-sectional area $A(p) \to A(p{+}\delta p)$. We estimate u_p by the total flux Q/A, i.e.

$$|\nabla_p u_p|^2 = 8\pi\alpha_2 \frac{Q^2}{A^4} \left|\frac{dA}{dx}\right|^2, \tag{8}$$

with proportionality factor α_2. Again, α_2 is intrinsically dependent on pore geometry and changes from pore to pore. We combine the two expressions Eq. (7) and Eq. (8) with Eq. (5) into

$$\frac{dp}{dx} = 8\pi\mu \frac{Q(p)}{A(p)^2} f\left(\alpha_i, \mathcal{S}(p)\right), \tag{9}$$

with

$$f\left(\alpha_i, \mathcal{S}(p)\right) = \alpha_0 + \alpha_1 \mathcal{C} + \alpha_2 \frac{1}{A} \left|\frac{dA}{dx}\right|^2. \tag{10}$$

This parametrization is consistent with the Hagen-Poiseuille equation for pipe geometries $f(\alpha_i) \to 1$, for which the local infinitesimal pressure gradient is given by

$$\frac{dp}{dx} = 8\pi\mu \frac{Q}{A^2}. \tag{11}$$

As long as the total flux Q remains constant and $dV = Adx$ remains valid, Eq. (9) can be integrated over Δp. We define a pore by the integrated volume, bound by iso-pressure surfaces $\mathcal{S}_i(p)$, $\mathcal{S}_j(p + \Delta p)$ and the porous media boundary. The hydraulic resistance of a pore is then given by $\mathcal{R} = \frac{\Delta p}{Q}$. The right-hand side of Eq. (5) gives us therefore a statistical model for the hydraulic resistance $\mathcal{R}_m$ is given by

$$\mathcal{R}_m = 8\pi\mu \int_0^{L_{\text{eff}}} \frac{1}{A^2} f\left(\alpha_i, \mathcal{S}(p)\right)\, dx, \tag{12}$$

with $L_{\text{eff}} = \int dx$ the total effective length of the pore. When the geometry of a media is given by a long pipe, the hydraulic resistance is given by the Hagen-Poiseuille (HP) model $\mathcal{R}_{\text{HP}}$, given by $\mathcal{R}_m(f \to 1)$. The HP model therefore only depends on the cross-sectional area $A(p)$.

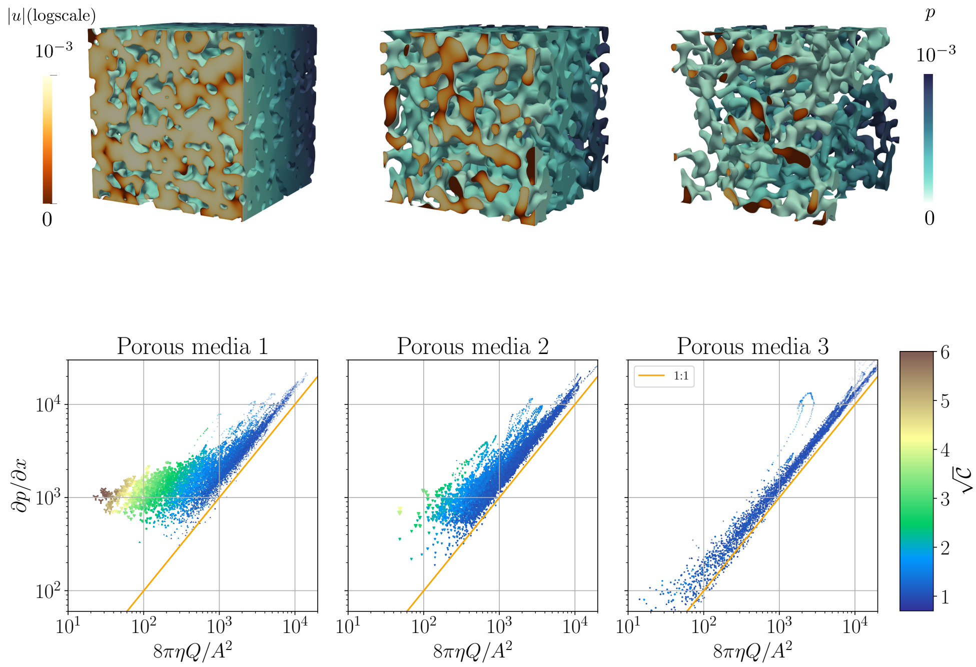

Figure 2: Top: A visualization of the velocity field $|u|$ and pressure field p in the pore space of the three porous media used in this study. Bottom: Measurements of local pressure drop versus the Hagen-Poiseuille model given by Eq. (11) for three different porous media. The color is given by averaged circularity $\mathcal{C}(p)_i$ and the marker size is scaled with the averaged area $A(p)_i$ of two consecutive iso-pressure surfaces $\mathcal{S}(p)_i, \mathcal{S}(p+\delta p)_j$.

3 Methods

To generate heterogeneous porous media we make use of the Gaussian Random Fields (GRF), which are increasingly used to represent realistic porous media (Liu et al., 2019). We used a fast Fourier transform and a spectral density function to generate GRF scalar functions (Teubner, 1991; Hyman et al., 2012; Siena et al., 2014). A threshold on the GRF function is used to define the porous media-fluid interface Γ with porosities $0.68, 0.34$ and 0.17 respectively. For details on the GRF functions and geometrical parameters such as average pore size and surface roughness are given in the SI. These porous media are used as input for direct numerical simulations (DNS, OpenFOAM v. 4.1, Weller et al. (1998)), that solve the Stokes equations (Eq. 1) in the pore space. The boundary conditions are defined at the inlet p_1 and outlet p_2 and a no-slip condition for the porous media-fluid interface. A visualization of the three porous media is shown in Fig. 2. Next, a chain of visualization toolkit (VTK) based image analysis techniques (Schroeder et al., 2006; Hernderson, 2007) is employed to extract iso-pressure surfaces $\mathcal{S}(p)$ and enumerate the disconnected areas identified as an iso-pressure patch $\mathcal{S}_i(p)$. This patch is part of a pore and has a surface area $A_i(p)$, circularity $\mathcal{C}_i(p)$, center of 'mass' of iso-pressure surface $\mathbf{X}_i(p)$ and total flux $Q_i(p)$. For each $\mathcal{S}_i(p)$ we identify its closest neighbor $\mathcal{S}_j(p+\delta p)$. This neighboring iso-pressure patch (building up a pore) is found by calculating the distance function $f_d(\mathbf{x}, \mathcal{S})$, between any given point $\mathbf{x} \in \mathcal{S}_i(p)$ and all iso-pressure patches $\mathcal{S}_k(p + \delta p)$. This distance function is defined by

$$f_d\left(\mathbf{x}, \mathcal{S}\right) = \min\{\|\mathbf{x} - \mathbf{y}\|\} \mid \mathbf{y} \in \mathcal{S}. \tag{13}$$

for each i, k we define the averaged distance matrix

$$d_{i,k} = \frac{1}{A_i(p)} \int_{\mathcal{S}_i(p)} f_d(\mathbf{x}_i, \mathcal{S}_k(p + \delta p))\, dS_i. \tag{14}$$

The closest neighbor $\mathcal{S}_j(p + \delta p)$ is found by the minimum value of $d_{i,j} = \min\{\mathrm{d_{i,k}}\}$. When δp is chosen sufficiently small the enclosed volume can be estimated by $V_i(p, \delta p) = A_i dx_i \approx A_i d_{i,j}$. We use forward integration of consecutive patches until merging or splitting takes place. This is translated into constraints on flux conservation and an upper bound for $d_{i,j}$. We noticed however that the distances between $\mathbf{X}_i(p)$ and $\mathbf{X}_j(p + \delta p)$ of two consecutive pores are more sensitive to topology changes, and are therefore used instead. The precise values for these constraints can be found in the SI. A demonstration of the correct identification of pores by forward integration is shown in Fig. 1 (Right), showing a merging of two pores. Although the proposed definition of individual pores deals naturally with junctions, a straight forward pore-network implementation is still missing. This is partly due to the exclusion of iso-pressure patches that are singular, and have no neighboring patches due to rapid changing topologies. The percentages of excluded surface area patches are 18%, 26% and 2%, which, at least for the first two porous media, prevents a continuous reconstruction of the network-topology. This is not an issue for the present work which aims at validating the novel constitutive relation on the level of individual pores and a continuous pore network is not required. However, for a pore-network implementation of the approach to be applicable, this should be resolved in future work.

The main challenge with the data format of the OpenFoam simulations is that it is unstructured, and the meshing is refined towards the boundary of the porous media Γ. Although this ensures that the geometry is accurately described and that the simulation converges, it also causes challenges in the extraction of $\mathcal{S}(p)$ by using a VTK contour filter. Since it is based on a threshold on p it breaks up the mesh close to Γ into many disconnected noisy area patches. These are removed by applying a filter on the area size of the patches, resulting in a reduction of total surface area of maximally 1%. Extracting circularity $\mathcal{C}_i(p)$ is achieved by applying a contour filter on $\mathcal{S}_i(p)$ with a threshold on the velocity of $|u| = 10^{-9}$ ms^{-1}, which is numerically zero.

For each of the three porous media we evaluate Eq. (9) for all consecutive iso-pressure pairs $\mathcal{S}_i(p)$. To obtain measured values for the resistance of a pore, we divide the total pressure difference Δp by the total flux Q. We fit Eq. (16), to all pores belonging to one porous media, yielding three sets of α_i.

4 Results

The result of the DNS for the three porous media is shown in Fig. 2. The Reynolds numbers are calculated by $\mathrm{Re} \sim \ell_\mathrm{p}\mathrm{q}/\nu$, with q the average flux through the porous media and ℓ_p the average pore size defined by the total porous media volume to total porous media interface ratio $\ell_p = 4\phi V/|\Gamma|$. For all porous media Re is smaller than 10^{-2}. In Fig. 2, bottom, the results of the infinitesimal pressure gradients versus the HP model (Eq. (11)) are shown. We observe that the HP model underestimates the pressure gradient by up to two orders of magnitude for the first porous media, to a relative good estimate for the third. We notice that $\mathcal{C}$ is the lowest for smallest pores, indicating that smaller iso-pressure surfaces are more circular than larger, more complex shaped iso-pressure surfaces. Besides the fact that the data covers different ranges we see no visual visual distinction between the three porous media, i.e. their data overlap and behave uniformly with respect to $\mathcal{C}$ and size A, see Fig. 3, top left.

For each porous media Eq. (9) has been fitted by minimizing the least-squared error independently to obtain estimates for α_i. The contribution of the term α_2 is insignificant for all three porous media and is reported in the SI. A simple fit, excluding α_2 resulted in three values for $\alpha_0 = 0.48, 0.52, 0.19$ and $\alpha_1 = 0.90, 0.87, 1.16$ for the corresponding porous media respectively. The result of the fitting is shown in Fig. 3 (top, right).

Using Eq. (9) with the fitted values for α_0 and α_1 ($\alpha_2 = 0$) we obtain a new model for local pore resistances $\mathcal{R}_m$, Eq. (16), which performs much better than the HP model. The result is shown in Fig. 3 (bottom, right). We notice that obtained values for α_1 are underestimated by $1/\epsilon$ given that the circularity is overestimated by ϵ.

The Pearson correlation coefficients R^2 for all models of the resistances are higher than 0.88. For the HP model the values for R^2 are given by $0.91, 0.88$ and 0.99. The coefficients R^2 of $\mathcal{R}_m$ are given by $0.97, 0.95$ and 0.99. The high values are caused by the large domain size spanning several orders of magnitude. The deviations of $\mathcal{R}_{\mathrm{HP}}$ with the measured values $\Delta p/Q$ are not uniform across the scales and therefore R^2 is not a reliable parameter when it comes to expressing the improvement over the HP model (Wilcox, 2009). We therefore calculated the reduction of the root-mean-squared-relative error (RMSRE) from $\mathcal{R}_{\mathrm{HP}}$ to $\mathcal{R}_{\mathrm{m}}$. For the first porous media we found a reduction in the RMSRE from 59% to 12%, for the second from 46% to 13% and for the last from 31% to 15%.

We visually observe that the circumferences of the iso-pressure surfaces are not smooth and lead to an overestimation of $\mathcal{C}_i(p)$. In the SI we have evaluated this error to be a factor $\epsilon = 1.15,\ 1.11,\ 1.08$ for the three porous media respectively. The origin of this error is the grid refinement near the boundary. Given that this is uniform throughout the porous media, we expect the error to be similar for all $\mathcal{C}_i(p)$. Considering this observation and the fact that the last term in Eq. 10 is insignificant, it is interesting to test the robustness of the linearity in $\mathcal{C}$ and the consistency of the function $f \to 1$ when $\mathcal{C} \to 1$. We introduce an alternative function g to f with two fit parameters α and β,

$$g(\mathcal{C}) = 1 - \alpha \left[1 - (\mathcal{C}/\epsilon)^{\beta}\right], \tag{15}$$

with a reduction factor $1/\epsilon$ for $\mathcal{C}$ to compensate for the known overestimation of $\mathcal{C}$. This function is consistent with the HP model as long as $\beta = 1$. The fitting resulted in three values for $\alpha = 0.45,\ 0.58,\ 0.34$, and $\beta = 1.09,\ 1.05,\ 1.08$. The latter suggesting that non-linear contributions of $\mathcal{C}$ can be present but are expected to be relatively small. A model including a quadratic term, reported in the SI, gives the same performance, but with the danger of over-fitting. By using $g(\mathcal{C})$ the RMSREs are higher than for the model resulting from fitting Eq. (16). This is reflected in a central spread of $\mathcal{R}_m$ around the $1:1$ line, whilst with Eq. (15), the model predicts generally values above the $1:1$ line. The Pearson correlation coefficients of the uniform model are similar, given by $R^2 = 0.97,\ 0.95$

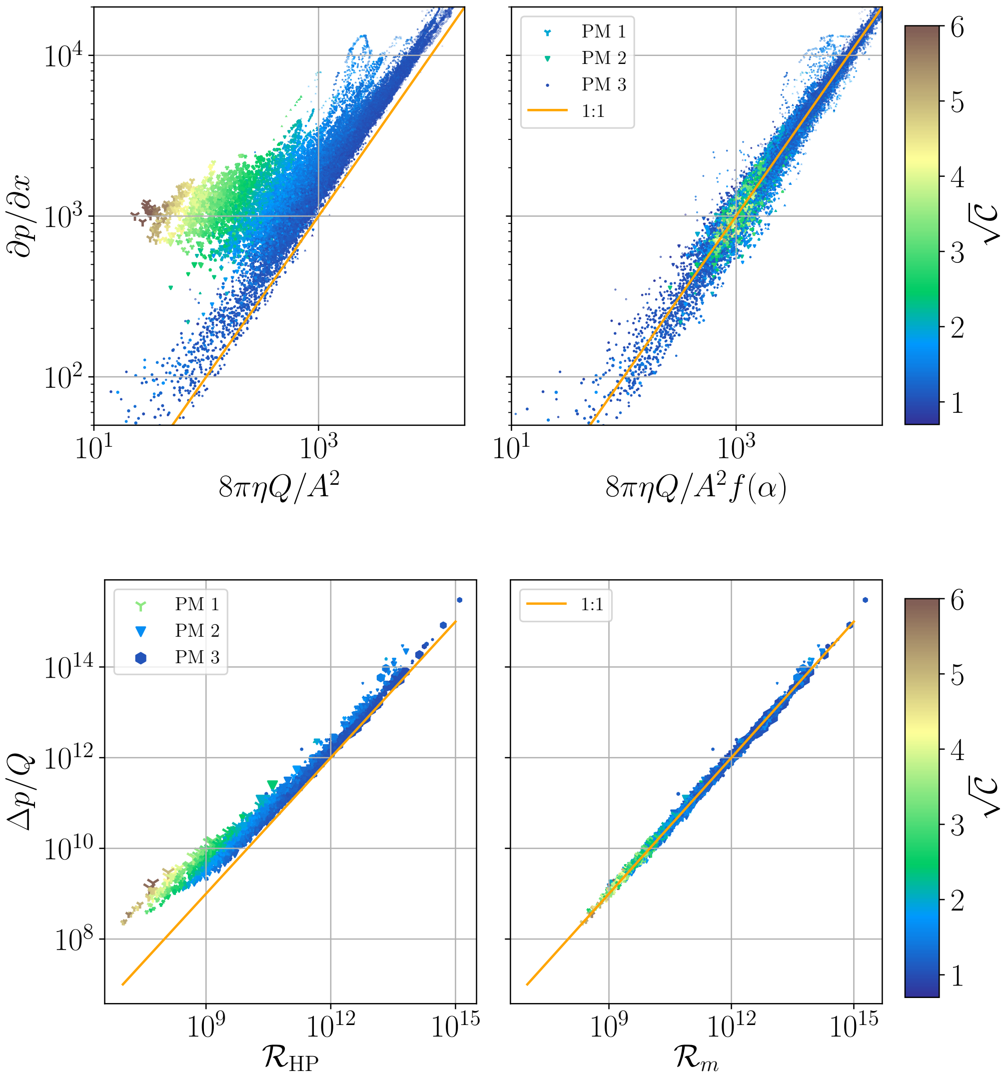

Figure 3: Top left: Measured infinitesimal pressure gradient versus the infinitesimal pressure drop of a Hagen-Poiseuille model, i.e. $f(\alpha) \to 1$, for all three porous media combined. The marker size is scaled with square root of the averaged area $\sqrt{A}$. Top right: Measured versus Modeled infinitesimal pressure gradient with $f(\alpha)$ fitted to Eq. (9) for each porous media separately. Bottom: The marker size is scaled by $N\sqrt{A}$, with N the number of consecutive patches. Bottom left: Integrated pressure drop vs $\mathcal{R}_{HP}$ times the total Flux Q. Bottom right: Integrated pressure drop divided by the total Flux Q vs $\mathcal{R}_m$ (Eq. (16)).

and 0.99 indicating a similar performance. All models and their parameters including performances are listed in the SI.

The range of local resistances in Fig. 3 (bottom) show that low resistances are correlated with high values for $\mathcal{C}$, and are poorly estimated by the HP model. These pores are crucial for predicting preferential flow paths since they depend on the paths of least resistances throughout a network. For this purpose we have computed the RMSRE weighted by the mean flux. We found a reduction from $86\%, 60\%, 32\%$ for the HP model to $10\%, 12\%, 13\%$ for the new model for the three heterogeneous media respectively, which shows a remarkable improvement for high flux pores.

5 Discussion

One of the most important findings is that the prediction of the resistance of a pore by $\mathcal{R}_{\mathrm{HP}}$ is highly underestimated with an average RMSRE of 0.45. This is most pronounced when the pores have a complex geometry, which are usually correlated with large pore areas, see Fig. 3. An average underestimation of the resistances leads to an average overestimation of the mean fluxes in a network model. This will affect transport predictions e.g. breakthrough times will be underestimated (Dentz et al., 2018). Network models such as (Alim et al., 2017), often base their local resistances on the smallest distances to the porous media boundary. In general this will underestimate the cross-sections and therefore obtain higher resistances for the HP-based model, potentially reducing the error with respect to our HP model. Since anomalous diffusion has been correlated with the degree of heterogeneity of the porous media, it is important that low flux regions are included. The inaccurate representation of the low velocity regions of larger cross-sectional areas will therefore contribute to poor estimates of anomalously long residence times. Estimating these residence times properly is important because they underly non-Fickian scaling behavior of the dispersion of flow tracers (Dentz et al., 2018; Dentz & Tartakovsky, 2006).

We expect that our main results are transferable to other media such as packed-beads, sandstone and disordered media, since iso-pressure surfaces are quite heterogeneous even if grains are regular. In ordered and/or high porosity media we expect iso-pressure surfaces that are highly connected, similar to porous media 1 in this paper, and sometimes even consisting of a singular patch. In these cases extracting statistics can be challenging. One possible strategy for separation of highly connected iso-pressure surfaces into smaller patches could be a watershed or Morse-Smale-Complex segmentation (Tierny et al., 2018).

One of the key observations of our work is the possibility of introducing a local geometric factor that provides for the ratio of pressure difference and mass flux in a given pore. The factor depends on the considered pore and not the rest of the complicated shape of the medium boundary. The non-triviality of this observation is made transparent by employing the boundary integral representation which is equivalent to the Stokes equations obeyed by the flow. The representation gives the flow as an integral over the medium surface where the points of the surface appear as sources that produce the flow as superposition. The "charge" of such sources is proportional to the stress tensor at the boundary and the flow that each charge induces in space is given by an appropriate Green's function, see e.g. (Pozrikidis, 1992). Our result demonstrates that contributions other than those from the boundary of the considered pore can be neglected in the superposition. The mechanism by which this occurs, consists of both screening effect and destructive interference between different pores. This deserves further studies which are beyond our scope here. We have used circularity, as a single measure for the shape of $\mathcal{S}(p)_i$, but to improve on this result it might be necessary to include other shape parameters such as curvature measures of $\mathcal{S}(p)_i$ and/or inclusion of a model for the boundary term (first term of Eq. 3), which however may lead to non-linear behavior in a circuit model.

Although a pore-network implementation is still missing due to the incomplete evaluation of all surface area patches, an alternative option is to use a statistical network representation based on our results. Given that the distributions of the resistances show similarity with a log-normal distribution (see SI), a pathway for a statistical network based on these distributions seems feasible.

6 Conclusion

We have proposed a new iso-pressure surface based definition for individual pores in heterogeneous porous media with the aim of measuring and modeling the local hydraulic resistance which can potentially be used in a pore-network model. This new definition uses the constant flux as constraint on the length of the pore. The definition of the pores allows us to estimate the local hydraulic resistance in terms of the viscous dissipation tensor. This can be modeled by Eq. (16), with $\alpha_2 = 0$ resulting in

$$\mathcal{R} = 8\pi\mu \int_0^{L_{\mathrm{eff}}} \frac{1}{A^2} \left(\alpha_0 + \alpha_1 \mathcal{C}\right) \, dx. \tag{16}$$

This model significantly improves the Hagen-Poiseuille model for heterogeneous media.

7 Data availability

The results of the DNS simulations and the results of the postprocessing on which the figures are based can accessed here (Krol, 2021).

Acknowledgments

The authors acknowledge support through SNSF grant nr.172916 and valuable discussions with H. Löwe and V. L. Morales.

References

Alim, K., Parsa, S., Weitz, D. A., & Brenner, M. P. (2017, October). Local Pore Size Correlations Determine Flow Distributions in Porous Media. *Phys. Rev. Lett.*, *119*(14), 144501. doi: 10.1103/PhysRevLett.119.144501

Bear, J. (1972). *Dynamics of fluids in porous media.*

de Anna, P., Quaife, B., Biros, G., & Juanes, R. (2017, December). Prediction of the low-velocity distribution from the pore structure in simple porous media. *Phys. Rev. Fluids*, *2*(12), 124103. doi: 10.1103/PhysRevFluids.2.124103

Dentz, M., Icardi, M., & Hidalgo, J. J. (2018, April). Mechanisms of dispersion in a porous medium. *Journal of Fluid Mechanics*, *841*, 851–882. doi: 10.1017/jfm.2018.120

Dentz, M., & Tartakovsky, D. M. (2006). Delay mechanisms of non-Fickian transport in heterogeneous media. *Geophysical Research Letters*, *33*(16). doi: 10.1029/2006GL027054

Dullien, F. A. L. (1975, January). Single phase flow through porous media and pore structure. *The Chemical Engineering Journal*, *10*(1), 1–34. doi: 10.1016/0300-9467(75)88013-0

Fatt, I. (1956, December). The Network Model of Porous Media. *Transactions of the AIME*, *207*(01), 144–181. doi: 10.2118/574-G

Fouxon, I., & Holzner, M. (2016, August). Solvable continuous-time random walk model of the motion of tracer particles through porous media. *Phys. Rev. E*, *94*(2), 022132. doi: 10.1103/PhysRevE.94.022132

Haring, R. E., & Greenkorn, R. A. (1970). A statistical model of a porous medium with nonuniform pores. *AIChE Journal*, *16*(3), 477–483. doi: 10.1002/aic.690160327

Hernderson, A. (2007). *ParaView Guide, A Parallel Visualization Application.*

Holzner, M., Morales, V. L., Willmann, M., & Dentz, M. (2015, July). Intermittent Lagrangian velocities and accelerations in three-dimensional porous medium flow. *Phys. Rev. E*, *92*(1), 013015. doi: 10.1103/PhysRevE.92.013015

Hyman, J. D., Smolarkiewicz, P. K., & Winter, C. L. (2012, November). Heterogeneities of flow in stochastically generated porous media. *Physical Review E*, *86*(5). doi: 10.1103/PhysRevE.86.056701

Katz, A. J., & Thompson, A. H. (1986, December). Quantitative prediction of permeability in porous rock. *Phys. Rev. B*, *34*(11), 8179–8181. doi: 10.1103/PhysRevB.34.8179

Krol, Q. (2021). *Hydraulic resistance of pores in porous media using DNS of laminar flow.* EnviDat.

Kutsovsky, Y. E., Scriven, L. E., Davis, H. T., & Hammer, B. E. (1996, April). NMR imaging of velocity profiles and velocity distributions in bead packs. *Physics of Fluids*, *8*(4), 863–871. doi: 10.1063/1.868867

Le Borgne, T., Bolster, D., Dentz, M., de Anna, P., & Tartakovsky, A. (2011, December). Effective pore-scale dispersion upscaling with a correlated continuous time random walk approach: EFFECTIVE PORE-SCALE DISPERSION UPSCALING. *Water Resour. Res.*, *47*(12). doi: 10.1029/2011WR010457

Liu, Y., Li, J., Sun, S., & Yu, B. (2019, October). Advances in Gaussian random field generation: A review. *Comput Geosci*, *23*(5), 1011–1047. doi: 10.1007/s10596-019-09867-y

Maier, R. S., Kroll, D. M., Davis, H. T., & Bernard, R. S. (1999, September). Simulation of Flow in Bidisperse Sphere Packings. *Journal of Colloid and Interface Science*, *217*(2), 341–347. doi: 10.1006/jcis.1999.6372

Mortensen, N. A., Okkels, F., & Bruus, H. (2005, May). Reexamination of Hagen-Poiseuille flow: Shape dependence of the hydraulic resistance in microchannels.

Physical Review E, *71*(5). doi: 10.1103/PhysRevE.71.057301

Pozrikidis, C. (1992). *Boundary Integral and Singularity Methods for Linearized Viscous Flow.* Cambridge: Cambridge University Press. doi: 10.1017/CBO9780511624124

Saffman, P. G. (1959, October). A theory of dispersion in a porous medium. *Journal of Fluid Mechanics*, *6*(3), 321–349. doi: 10.1017/S0022112059000672

Scheidegger, A. E. (1974). *The Physics of Flow Through Porous Media (3rd Edition).* University of Toronto Press.

Schroeder, W., Martin, K., & Lorensen, B. (2006). *The visualization toolkit: An object-oriented approach to 3D graphics* (4. ed ed.). Clifton Park, NY: Kitware, Inc.

Siena, M., Riva, M., Hyman, J. D., Winter, C. L., & Guadagnini, A. (2014). Relationship between pore size and velocity probability distributions in stochastically generated porous media. *Phys. Rev. E*, *89*(1), 013018. doi: 10.1103/PhysRevE.89.013018

Teubner, M. (1991). Level Surfaces of Gaussian Random Fields and Microemulsions. *EPL (Europhysics Letters)*, *14*(5), 403.

Thompson, K. E., & Fogler, H. S. (1997). Modeling flow in disordered packed beds from pore-scale fluid mechanics. *AIChE Journal*, *43*(6), 1377–1389. doi: 10.1002/aic.690430602

Tierny, J., Favelier, G., Levine, J. A., Gueunet, C., & Michaux, M. (2018, January). The Topology ToolKit. *IEEE Transactions on Visualization and Computer Graphics*, *24*(1), 832–842. doi: 10.1109/TVCG.2017.2743938

Weller, H. G., Tabor, G., Jasak, H., & Fureby, C. (1998, December). A tensorial approach to computational continuum mechanics using object-oriented techniques. *Computers in Physics*, *12*(6), 620. doi: 10.1063/1.168744

Wilcox, R. R. (2009, November). Comparing Pearson Correlations: Dealing with Heteroscedasticity and Nonnormality. *Communications in Statistics - Simulation and Computation*, *38*(10), 2220–2234. doi: 10.1080/03610910903289151

Xiong, Q., Baychev, T. G., & Jivkov, A. P. (2016, September). Review of pore network modelling of porous media: Experimental characterisations, network constructions and applications to reactive transport. *Journal of Contaminant Hydrology*, *192*, 101–117. doi: 10.1016/j.jconhyd.2016.07.002

Supporting Information for "Local lydraulic conductivity in heterogeneous porous media"

Quirine Krol [1], Itzhak Fouxon [1,2], Pascal Corso [1], Markus Holzner [1,3,4]

[1]ETH Zurich, Stefano Franscini-Platz 5, 8093 Zurich, Switzerland

[2]Department of Computational Science and Engineering, Yonsei University, Seoul 120-749, South Korea

[3]Swiss Federal Institute for Water Science and Technology EAWAG

[4]Swiss Federal Institute for Forest, Snow and Landscape Research WSL

Contents of this file

1. Direct numerical simulation of Stokes flow in porous media and extraction of pore attributes.
2. Fitting models, results and model performance.
3. Measuring the contribution of the boundary term to Eq.(3).
4. Measuring the Transversal and Longitudinal Energy Dissipation tensor.
5. Histograms of L_{eff} and resistances $\mathcal{R}$.

Introduction

Below we describe the necessary steps and specific settings of the analysis presented in methodology. The fist part consists of the description of the direct numerical simulations performed that are used as a numerical experiment, followed by details of the extraction of iso pressure surfaces and and their attributes necessary to calculate the pore resistance. The second part gives the details involving models, including a detailed overview of their performance. In the third section we show with an example that Eq.(6) is a reasonable assumption. In the last section we show the distributions of the local resistances and the integrated pore lengths and a very short description of a roadmap describing a possible application of a network model approach.

1. Direct numerical Simulations and extraction of pore attributes

1.1. Geometry of the porous media interface

For all 3 media we have used a levelset of a Gaussian Random Field given by a spectral density as given in (Roberts & Teubner, 1995). Gaussian Random Fields are increasingly used for modeling porous media (Liu et al., 2019). The porous media boundary is given by a level-set and was chosen such that we have porosity values of $0.68, 0.34$ and 0.16, for porous media 1, 2 and 3 respectively. The geometries are represented by 3 stl files that serve as input for the build-in meshing algorithm of Openfoam v. 4.1 Weller, Tabor, Jasak, and Fureby (1998). The bounding box of the porous media (inlet, outlet, upper and lower wall, front and back) are obtained with a BlockMesh. The meshing of the pore space is obtained with SnappyHexMesh with refinement levels 2, for a minimum and 3 for a maximum at the porous media boundary. The number of cells are $35, 31,$ and15 Million respectively.

We inlcuded Table 1.1 that show a few geometrical parameters characterizing the porous media. The averaged pore size is defined by $l_p = 4\phi/s$ with $s = |\Gamma|/V$ the specific surface area given by the ratio of porous media interface total area $|\Gamma|$ and the total volume V. The relative pore size ℓ_p/L, with L the porous media extend. The surface roughness is defined by the standard deviation of the mean curvature H divided by the average pore size l_p. These measures are introduced to show the wide range of chosen geometries. For example the roughness is smaller for the first porous media compared to the other two. This might indicate that the circularity of the iso-pressure surfaces will be higher, and will have a larger impact on the local hydraulic resistance.

-	porosity	s	l_p/L	$\mathrm{std(H)^{-1}/l_p}$
PM1	0.68	2.0×10^4	0.17	0.14
PM2	0.34	1.8×10^4	0.08	0.44
PM3	0.17	1.2×10^4	0.06	0.35

1.2. Direct Numerical Simulations

The flow in the three porous medium configurations was simulated using the open-source OpenFOAM software . The three-dimensional meshes consisting in the majority of hexahedral cells were generated from the surface of the porous media represented as a tessellation of triangles. The meshes were obtained using the build-in SnappyHexMesh utility. For the three configurations, the meshes consist of approximately 10 million cells and the non-orthogonality between the faces of each cell is limited to 60and the skewness (as defined within OpenFOAM) of the cells is at most equal to 4 (Moukalled et al., 2016). The steady-state Navier-Stokes equations are resolved using the SIMPLE algorithm for coupling the pressure and momentum equations (Jasak, 1996). Relaxation factors were chosen to be equal to 0.7 for the momentum equation and 0.2 for the pressure equation in order to ensure stability. The choice of the spatial discretization schemes is made such that the simulations are second-order accurate. For the diffusive term, which is dominating for the range of Reynolds numbers considered in these simulations, a limiter for the computation of gradient at the interface between two cells is introduced to take into account the effect of cell non-orthogonality and skewness and at the same time to keep the solution bounded.

Concerning boundary conditions, the velocity at the pore surface is set to zero. A pressure difference of 1 Pa at the two extremities perpendicular to the stream-wise direction of the box defining the computational domain is imposed. The dimension of the box in this direction is 1 mm. The lateral faces of the computational box are also associated with a zero-velocity condition. The simulations are initialized with PotentialFoam and run with SimpleFoam with standard residual controls of 10^{-6} for both the pressure and velocity fields. The Kinematic viscosity is set to $10^{-6}\mathrm{m}^2\mathrm{s}^{-1}$, which is close to the value for water. The SimpleFoam solver took approximately 20, 8 and 3 hours to obtain the results using 32 cores. A visualization of the results for the three porous media is shown in Fig.2 of the main manuscript.

1.3. Extraction of pores based on iso-pressure surfaces

A chain of VTK-based image analysis techniques Schroeder, Martin, and Lorensen (2006); Hernderson (2007) is employed to extract iso-pressure surfaces. The analysis is scripted with pvpython which comes with the Topology ToolKit (TTK) installation for MACOS High Sierra (python 2.7.15, Paraview 5.4.1, TTK 0.9.3) (Tierny et al., 2018). Specific Paraview/TTK filters are denoted with a capital letter. Values for parameters are given without units, but can be inferred from its definition. Note that the results of the simulation assign p with the kinematic pressure, i.e. in units $\mathrm{m}^2\mathrm{s}^{-2}$, from which the derive the static pressure by multiplication with the fluid density $p_s = p\rho_f$. The results in the paper are in correct units (using Pa for p), but in the following keep p as the kinematic pressure.

Iso-pressure surfaces $\mathcal{S}(p)$ and noise removal

- The iso-pressure surfaces $\mathcal{S}(p)$ are obtained by taking a contour (Contour) filter on pressure value p on the DNS data, see Fig. S1 (left). For porous media 1 and 2 we have chosen k iso-pressure surfaces $p_k = p_0 + k\delta p$ with $\delta p = 5 \times 10^{-6}$. Due to large heterogeneity in the pressure gradient in the third porous media we have chosen to double its resolution to $\delta p = 2.5 \times 10^{-6}$. Due to the noisy edges, as described in the paper, we remove small area patches. This is done by segmenting $\mathcal{S}(p_k)$ with the Connectivity filter in $j \in \{1, M_k\}$ disconnected patches $\mathcal{S}_j(p_k)$ with total area $A_0(p_k)$. Each patch is isolated by a Threshold filter and its surface area $A_j(p_k)$ determined by an IntegrateVariables filter. A maximum value for $A_j(p_k) > A_{\min}$ is used to append (AppendGeometry) to construct $\mathcal{S}(p_k)$ with total area A_{total} consisting of N_k iso-pressure surface patches. The value $A_{\min}$ is determined by a sensitivity study on the total remaining area A_k and the number N_k of remaining patches as a function of $A_{\min}$. The threshold values are $A_{\min} = 3 \times 10^{-11}, 5 \times 10^{-11}$ and 2×10^{-12} for the PM respectively and are determined from Fig. S2 showing A_{total}/A_0 and N/A_0 as a function of $A_{\min}$ for three independent values of p_k. An example of $\mathcal{S}_i$ is shown in Fig. S1 (left). The reduction of the total area has been at most 1.5% for these three test iso-pressure surfaces.

- For $i = 0$ and $i = N$, the iso-pressures surfaces are flat. Since we deem this to be a finite size effect and in this case 'unnatural' we allow the iso-pressure surfaces to develop over the first and last 10 slices, defining p_0.

- To repair some of the irregularities in the surface mesh we employ three more filters: Tetrahydralize, CleantoGrid, and an ExtractSurface.

Segmentation of $\mathcal{S}_i(p_k)$

- To segment $\mathcal{S}_i(p_k)$ into $i \in 1, N_k$ individual pores $\mathcal{S}_i(p_k)$ a connectivity filter is applied (Connectivity, enumeration named 'RegionId'), followed by a ExtractSurface and GenerateSurfaceNormals filter. An example of a segmentation is shown in Fig. S1 (middle).

- To obtain the circularity $\mathcal{C}_i(p_k)$ we take a Contour on numerically zeros velocity $|u| = 10^{-9}$m/s. The obtained contour is subsequently integrated to obtain $\mathcal{L}_i(p_k)$.

By visual inspection of the iso-pressure surfaces (using Paraview software) we see that the circumferences are irregular and will lead to an overestimation of $\mathcal{C}_i(p_k)$. To investigate the dependency of $\mathcal{L}$ on the magnitude $|u|$ we performed a sensitivity study, see Fig.(S2). We found that although the circumferences are visually smoother for higher values of $|u|$ (See third row of Fig S2), fundamental shape features get lost before the smoothing is significant, and can therefore not be used. Choosing $|u| = 10^{-9}$m/s gives us the closest boundary representation of the porous media boundary wall. Choosing $|u| < 10^{-9}$m/s does not lead to higher measured circumferences, this value is therefore numerically zero. Choosing a higher value for the threshold would lead to slightly smoother circumferences (a reduction in $\mathcal{L}$), but with that we also loose qualitative features of the circumferences e.g. a change in topology leads to an increase in the circumferences observed in PM1 and PM2 (See Fig. S2). From this sensitivity study we cannot define a higher value for the threshold that would lead to a better estimate for the circumferences whilst keeping the quality of the shape. Therefore we estimate the error via an alternative method and choose to reduce all the circumferences by this factor.

- **overestimation of $\mathcal{C}_i(p_k)$.** To estimate the order of overestimation regarding $\mathcal{C}_i(p_k)$, we have done a control study by comparing the circumference obtained by thresholding the porous media boundary directly on pressure p_k. This yields a total circumference of iso-pressure surface $\mathcal{S}(p_k)$. Comparing this to $\sum_i^{N(k)} \mathcal{C}_i(p_k)$, with $N(k)$ the total number of iso-pressure pathces of iso-pressure surface $\mathcal{S}(p_k)$, gives us an averaged overestimation of $\mathcal{C}_i(p_k)$ by a factor $\epsilon = 1.15 \pm .01, 1.11 \pm .01$, and $1.08 \pm .04$, for the three porous media respectively. This estimate is based on 40 iso-pressure surfaces taken from each porous media.

- For each $\mathcal{S}_i(p_k)$ we integrate (IntegrateVariables) the surface to extract the averaged position $\mathrm{X}_i(p_k)$, total flux $Q_i(p_k) = \int_{\mathcal{S}_i(p_k)} \mathbf{u} \cdot \mathbf{n}\, da$, and total area $A_{i,j} = \int_{\mathcal{S}_i(p_k)} da$ and circularity $\mathcal{C}_i(p_k) = \mathcal{L}_i^2(p_k)/(4\pi A_i(p_k))$.

Local inheritance $\mathcal{S}_i(p)$

Goal: For each $\mathcal{S}_i(p_k)$ finding its closest neighbor $\mathcal{S}_j(p_k + \delta p)$.

-]This neighboring iso-pressure patch (building up a pore) is found by calculating the distance function $f_d(\mathbf{x}, \mathcal{S})$, between point $\mathbf{x} \in \mathcal{S}_i(p_k)$ and all iso-pressure patches $\mathcal{S}_l(p_k + dp)$. This distance function is calculated by the vtkDistancePolyDataFilter, a programmable vtk filter, and is defined by

$$f_d\,(\mathbf{x}, \mathcal{S}) = \min\{\|\mathbf{x} - \mathbf{y}\|\}|\mathbf{y} \in \mathcal{S}. \tag{1}$$

for each i, l we define the averaged distance matrix by using the IntegrateVariables filter

$$d_{i,l}(p_k) = \frac{1}{A_i(p_k)} \int_{\mathcal{S}_i(p_k)} f_d(\mathbf{x}_i, \mathcal{S}_l(p_k + \delta p))\, dS_i. \tag{2}$$

The closest neighbor $\mathcal{S}_j(p_k + \delta p)$ is found by the minimum value of $d_{i,j}(p_k) = \min\{\mathrm{d_{i,l}(p_k)}\}$. The closest neighbor is assigned by the identification number of the nearest neighbor $n_i(p_k) = j$

- Subsequently we compute the change in surface area $dA_i(p_k) = A_i(p_k) - A_j(p_k + \delta p)$, the averaged location of the neighboring pore $\mathbf{X}_i^n(p_k) = \mathbf{X}_j(p_k + \delta p)$ and the distances between the two averaged coordinates $dX_i(p_k) = |\mathbf{X}_i(p_k) - \mathbf{X}_j(p_k + \delta p)|$. Last but not least we assign $dx_i(p_k) = d_{i,j}(p_k)$, which is used as dx in the Eq. (10) and (12).

- Now each patch $\mathcal{S}_i(p_k)$ has intrinsic attributes enlisted: $i, n_i, \mathbf{X}_i$, Q_i, A_i, $\mathcal{C}_i$. Additionally it has attributes that depend on its nearest neighbor n_i, $\mathbf{X}_i^n$, dA_i, dx_i and dX_i. For all these attributes p_k is implied. The intrinsic attributes of the nearest neighbor are added to the attributes of $\mathcal{S}_i(p_k)$ for convenience.

- It is important to notice the difference between dx_i and dX_i. The former is the averaged distance between two iso-pressure surface patches and therefore assigned to dx wich stems from $dV = Adx$. The latter is the distance between the two averaged positions of the iso-pressure patches.

- Gathered all necessary pore attributes, we can use a least-squared fit of Eq.(9) to obtain α_i and Eq.(15) to obtain α and β.

Defining pores by integration of local inheritance of $\mathcal{S}_i(p)$

• For the first iso-pressure patches $S_i(p_0)$ we initiate a pore identification number $P_i(p_k) = i$.

• For each pore i we integrate to the nearest neighbor j by assigning the same pore number to $\mathcal{S}_{n_i}(p_0 + \delta p) :\ P_{n_i}(p_0 + \delta p) = i$. This forward integration takes place only when five quality factors are fulfilled,

• $Q_1 = (|dX_i - dX_{n_i}|)/dX_i < q_1$: Ensuring that there is no abrupt change in consecutive averaged distances.

• $Q_2 = |dA_i|/A_i < q_2$: Ensuring no abrupt changes in the surface area of consecutive area patches.

• $Q_3 = (|Q_{0,j} - Q_{1,nn_{i,j}}|)/Q_{1,nn_{i,j}} < q_3$: Ensuring that the flux is 'nearly' conserved.

- $Q_4 = dX_i < q_4$: Ensuring that pores split if they are too far apart.

- $Q_5 = A_i > q_5$: Removing 'small' area patches. The values are found by trial and error to decrease the number of pores but still capturing the merging and splitting of pores. For each quality factor we have 3 values tailored to each porous media 1,2 and 3 independently. For $q_1 = [1.6, .4, .4]$, $q_2 = [.5, .5, 1]$, $q_3 = [.2, .2, 1]$, $q_4 = [10^{-5}, 10^{-5}, 9 \times 10^{-5}]$ and $q_5 = [1 \times 10^{-10}, 1 \times 10^{-10}, 5 \times 10^{-11}]$ These requirement seem quite loose, but have proven to be quite effective, see Fig. S1 (Right).

- The assignment of pore numbers can continue iteratively until all patches have a pore identification number $P_i(p_k)$.

- For all P_i we can calculate Eq.(12) and Eq.(15).

2. Fitting models, Results and Performance

2.1. Fitting models

In the paper we have fitted four models f_i

$$\frac{dp}{dx} = \frac{Q}{A^2} f_i \tag{3}$$

for all consecutive pore patches that comply with the the quality factors Q_i, not to be mistaken with averaged flux. Since the data is spread over multiple orders of magnitude, we obtained a least squared fit by taking the logarithm on either side of the equation

$$\log\left[\frac{dp}{dx}\right] = \log\left[\frac{Q}{A^2} f_i\right] \tag{4}$$

The 4 functions that have been fitted are given by

$$f_{\mathrm{HP}} = 1$$

$$f_1 = \alpha_0 + \alpha_1 \mathcal{C} + \alpha_2 \frac{1}{A}\left|\frac{dA}{dx}\right|^2$$

$$f_2 = \beta_0 + \beta_1 \mathcal{C}$$

$$f_3 = 1 - \alpha \left[1 - (\mathcal{C}/\epsilon)^{\beta} \right].$$

$$f_4 = \gamma_0 + \gamma_1 (\mathcal{C}/\epsilon) + \gamma_1 (\mathcal{C}/\epsilon)^2.$$

For f_3 and f_4 we have used an overall correction factor for $\mathcal{C}$ specific to each porous media as reported in the paper. We have included one additional condition that $dp/dx > 0.8\frac{Q}{A^2}$, to ensure that unphysical measurements of the pressure gradient. This can be caused by wrongly matched patches. This led to a reduction in evaluated surface areas of 0.4%, 0.3% and 2.6% for the porous media respectively. In addition singular patches that have not been matches are contributing to respectively $18\%, 26\%$ and 1.7% of the evaluated surface areas.

2.2. Results 1

Summary of fitting parameters and error measures for porous media 1

model	parameters	relative contributions	R^2
f_{HP}	-	[100%]	0.91
f_1	$\alpha_0 = 0.48, \alpha_1 = 0.90, \alpha_2 = -6.3 \times 10^{-7}$	$[23\%, 77\%, < .1\%]$	0.98
f_2	$\beta_0 = 0.48, \beta_1 = 0.90$	$[23\%, 77\%]$	0.97
f_3	$\alpha = 0.45, \beta = 1.09$	-	0.97
f_4	$\gamma_0 = 0.53, \gamma_1 = 1.18, \gamma_2 = 9.5 \times 10^{-3}$	$[25\%, 73\%, 1\%]$	0.98

Summary of fitting parameters and error measures for porous media 2

model	parameters	relative contributions	R^2
f_{HP}	-	[100%]	0.97
f_1	$\alpha_0 = 0.52, \alpha_1 = 0.87, \alpha_2 = 1.1 \times 10^{-6}$	$[31\%, 69\%, < .1\%]$	0.99
f_2	$\beta_0 = 0.52, \beta_1 = 0.87$	$[31\%, 69\%]$	0.99
f_3	$\alpha = 0.58, \beta = 1.05$	-	0.98
f_4	$\gamma_0 = 0.71, \gamma_1 = 0.65, \gamma_2 = 0.06$	$[42\%, 51\%, 8\%]$	0.99

Summary of fitting parameters and error measures for porous media 3

model	parameters	relative contributions	R^2
f_{HP}	-	[100%]	0.94
f_1	$\alpha_0 = 0.26, \alpha_1 = 1.07, \alpha_2 = 6.3 \times 10^{-5}$	$[18\%, 82\%, < .1\%]$	0.97
f_2	$\beta_0 = 0.26, \beta_1 = 1.07$	$[18\%, 82\%]$	0.97
f_3	$\alpha = 0.34, \beta = 1.08$	-	0.97
f_4	$\gamma_0 = 2.1, \gamma_1 = -2.1, \gamma_2 = 1.4$	$[148\%, -136\%, 88\%]$	0.96

2.3. Results 2

The model performance have been expressed in the Pearson correlation coefficient R^2 of the measured $\mathcal{R}_{\mathrm{meas}} = \Delta p/Q$ and the modeled,

$$\mathcal{R}_{\mathrm{m}}(f_i) = \int_0^{L_{\mathrm{eff}}} \frac{1}{A^2} f_i(\mathcal{C})\, dx, \tag{5}$$

and the HP model

$$\mathcal{R}_{\mathrm{HP}} = \int_0^{L_{\mathrm{eff}}} \frac{1}{A^2}\, dx. \tag{6}$$

Since the errors between $\mathcal{R}_{\mathrm{meas}}$ and $\mathcal{R}_{\mathrm{HP}}$ shows a high degree of heteroscedasticy (Wilcox, 2009), the Pearson correlation function is not adequate to compare these models, therefore we also computed the root-mean-square-relative error (RMSRE). To investigate the potential improvement on preferential channels (those with low resistances or high fluxes), we weighted the RMSRE with the total flux Q through the pore, $\mathrm{RMSRE_Q}$. The results are shown in the following tables for the three porous media respectively.

Summary model hydraulic resistance performance for porous media 1:

model	R^2	RMSRE	$\mathrm{RMSRE_Q}$
$\mathcal{R}_{\mathrm{HP}}$	0.91	0.59	0.86
$\mathcal{R}_{\mathrm{m}}(f_2)$	0.97	0.12	0.10
$\mathcal{R}_{\mathrm{m}}(f_3)$	0.97	0.32	0.27

Summary model hydraulic resistance performance for porous media 2:

model	R^2	RMSRE	RMSRE_Q
$\mathcal{R}_\text{HP}$	0.88	0.48	0.61
$\mathcal{R}_\text{m}(f_2)$	0.95	0.14	0.13
$\mathcal{R}_\text{m}(f_3)$	0.95	0.28	0.29

Summary model hydraulic resistance performance for porous media 3:

model	R^2	RMSRE	RMSRE_Q
$\mathcal{R}_\text{HP}$	0.99	0.32	0.32
$\mathcal{R}_\text{m}(f_2)$	0.99	0.17	0.15
$\mathcal{R}_\text{m}(f_3)$	0.99	0.28	0.20

3. Measuring the relative contribution of the boundary term to Eq.(3)

In this section we estimate the relative contribution of the first term of the right-hand side of Eq.(3) of the manuscript, given by

$$Q\Delta p = -\mu \int_{S_{p_1}+S_{p_2}} \mathbf{u} \cdot (\nabla \otimes \mathbf{u})\mathbf{n}\, dS + \mu \int_{\mathcal{V}} (\nabla \otimes \mathbf{u})^2 dV. \tag{7}$$

We manually selected 10 pores (5 for porous media 1, 4 for porous media 2 and one for porous media number 3), and measured the ratio of the absolute value of the first term of the right-hand side and the left-hand side of the equation.

$$\text{ratio} = \frac{\left| -\mu \int_{\text{S}_{\text{p}_1}+\text{S}_{\text{p}_2}} \mathbf{u} \cdot (\nabla \otimes \mathbf{u})\mathbf{n}\, \text{dS} \right|}{\text{Q}\Delta\text{p}} \tag{8}$$

for varying lengths of the pore. Using a gradient filter, GradientOfUnstructuredDataSet, to extract the dissipation tensor $\partial_i u_j$. Note that gradients aren't used throughout the methods in this paper because they are less reliable since the the gradients increase the noise compared to the noise of the velocity data (see next section). Since the noise on the gradients lead to an overestimation of the ratio. This is not problematic for this purpose since we search for an upper value for its contribution. We have plotted all possible lengths that fit within one pore e.g. if a pore comprises 20 pores, we can measure 5 pores of length 15, by moving the window. In Fig. S3 we have plotted the ratio of the first term for all possible pores (left) with varying pore size for 10 available pores with respect to the left-hand side of the equation $Q\Delta p$. In Fig.3 (right) we have plotted the averaged ratios. We find that almost all ratios are well below 10% and that on average the ratio is below 5%. Almost all pores show that this ratio decreases roughly exponentially, reducing by half after a pore length of 7-10 units. Pore lengths are here expressed in Δp.

4. Measuring the relative Longitudinal and Transversal energy dissipation on an iso-pressure surface

In the theoretical section of the paper we have derived expressions for the longitudinal and transversal energy dissipation tensors, by

$$|\nabla_i u_j|^2 \approx |\nabla_s u_p|^2 + |\nabla_n u_p|^2 . \tag{9}$$

where we have assumed that the terms $|\nabla_n u_n|^2$ and $|\nabla_s u_n|^2$ are negligible. We will show two examples where we have calculated the individual terms of the total viscous dissipation. Because the highest dissipation is expected to be located near the porous media interface and the discretization also refined at the interface the numerical noise is also expected to be higher, see Fig S4. All 3 porous media contain some points in the mesh where the VTK gradient filter can't factorize the linear system which leads to very high values of the respected fields, See fig S4. The origin lies likely in the mesh quality generated by the snappyHexMesh generator contained in the openFoam simulation. Since the simulations have all converged we do not question the original simulation results but we do note that post-processing of these meshes can be difficult especially if gradients have to be calculated. Nevertheless we have tried to quantify the relevance of the transversal and longitudinal terms of the viscous dissipation tensor. We have chosen to threshold the unreasonable high gradient terms based on outliers in the histograms of the gradients. For the first porous media the porous media the refinement was chosen a degree higher than the others, and led to 'nan' results of the integrated relative contributions. For the two other porous media we have found reasonable results given in Table S3. Since we have to filter out quit some data that exhibits unreasonable high values the percentages are not adding up to 100%. By visual inspection we can examine the term $|\nabla_i u_j|^2$ in all porous media and we see that the total dissipation correlates with gradients in the transverse direction. Also in this data we can see that for Porous Media 3 the relative contribution of the longitudinal term $|\nabla_n u_p|^2$, 24% is in the same order as the transversal term $|\nabla_s u_p|^2$ which amounts to 32%. This observation is in agreement with the fitting of the two contributions in the paper, See Table S1.

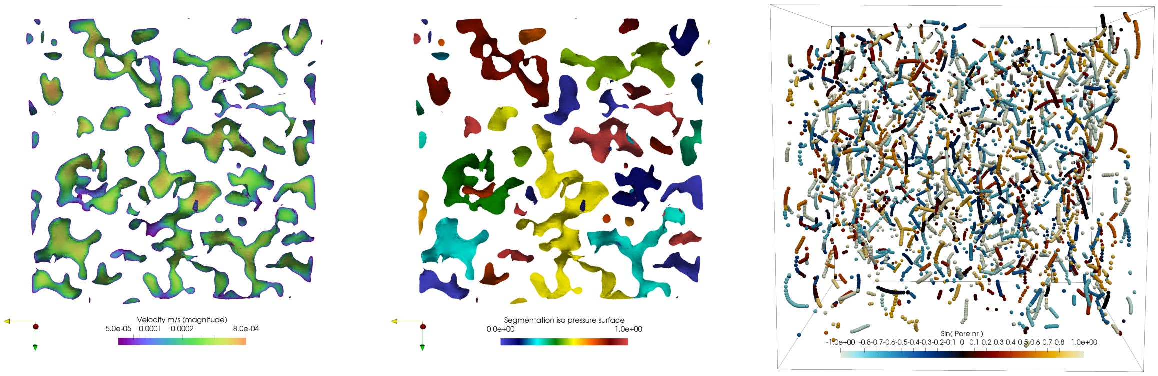

Figure S1. Visualization of left: velocity field $|\mathbf{u}|$of an iso-pressure surface $\mathcal{S}(p)$ at pressure value p, middle: segmentation into iso-pressure patches $\mathcal{S}_i(p)$, right: Pore identification throughout the porous medium.

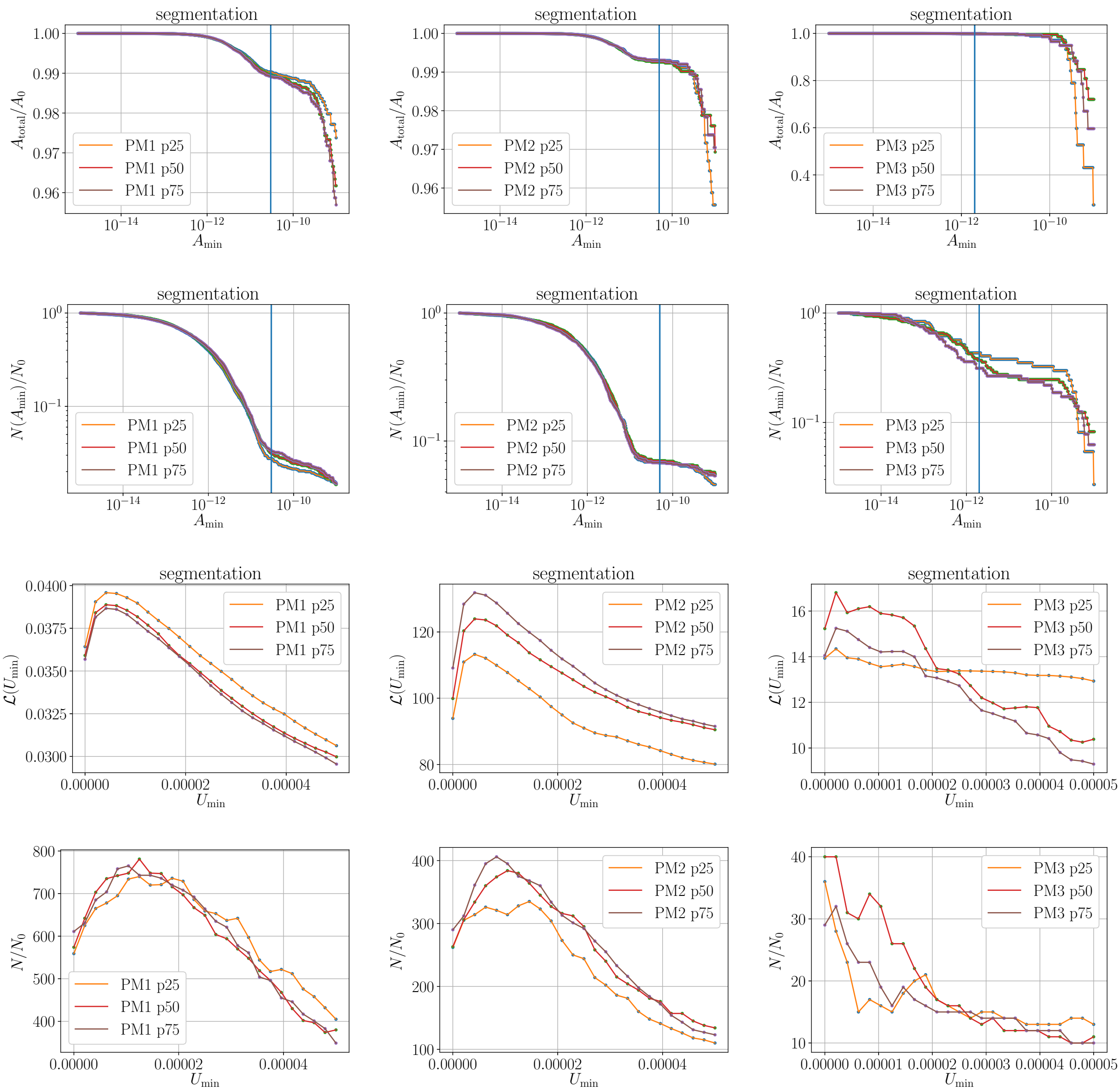

Figure S2. First row: Sensitivity study of total area A as a function of A_{min}. Second row: Sensitivity study of the number of patches N as a function of A_{min}. Third row: Sensitivity study of the total length of the circumference of three the iso-pressure surfaces $\mathcal{S}(p)$, $\mathcal{L}$ as a function of U_{min}. Fourth row: Sensitivity study of the total number of iso-pressure 'patches' $\mathcal{S}_i(p)$, N as a function of U_{min}.

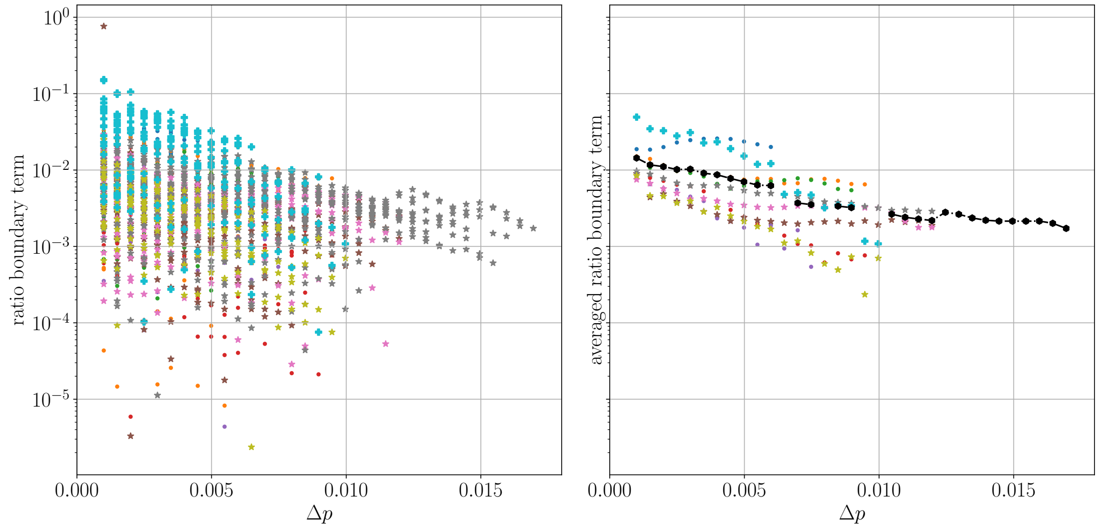

Figure S3. Left: Ratio of the boundary term to $Q\Delta p$ (first term of the right-hand side of Eq.(3) of the manuscript) as a function of the pore length (expressed in Δp) for 10 pores (bullets for pores from PM1, stars for pores from PM2, and squares for the pore of PM2). Right: The averaged ratio (averaged over all pore lengths within one pore (term 2 of the right-hand-side) as a function of pore length. In black the averaged value over all pores.

PM	$\lvert\nabla_s u_p\rvert^2$	$\lvert\nabla_n u_p\rvert^2$	$\lvert\nabla_n u_n\rvert^2$	$\lvert\nabla_n u_n\rvert^2$
PM2	71%	17%	12%	12%
PM3	32%	24%	10%	5%

Table S1. Estimated relative contributions to the total viscous dissipation on an iso-pressure surface.

5. Histograms of $\mathcal{R}$ and L_{eff}

In Fig. S5 we plotted the histograms of measured hydraulic resistances $\mathcal{R}_{\text{meas}}$, HP model $\mathcal{R}_{\text{HP}}$, and our model $\mathcal{R}_{\text{m}}(f_2)$. In Fig. S6 we have shown the histograms of L_{eff}. The plots include a Kernal Density Estimate (KDE) of the distributions. These distributions could potentially be

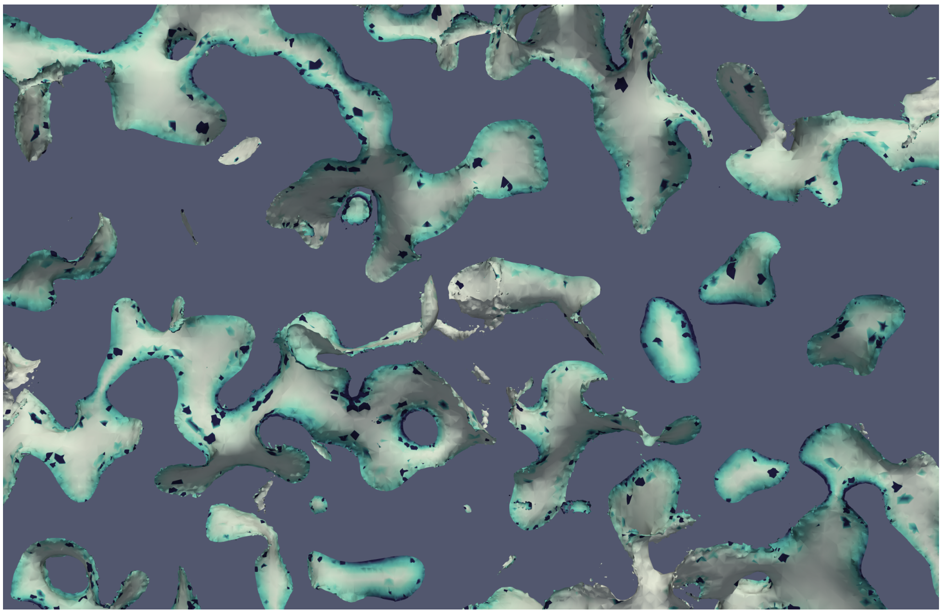

Figure S4. A visualization of the energy dissipation tensor $|\nabla \otimes \mathbf{u}|$ on a iso-pressure surface of PM1, indicating the numerical issues that are accompanied by gradients of the velocity vector.

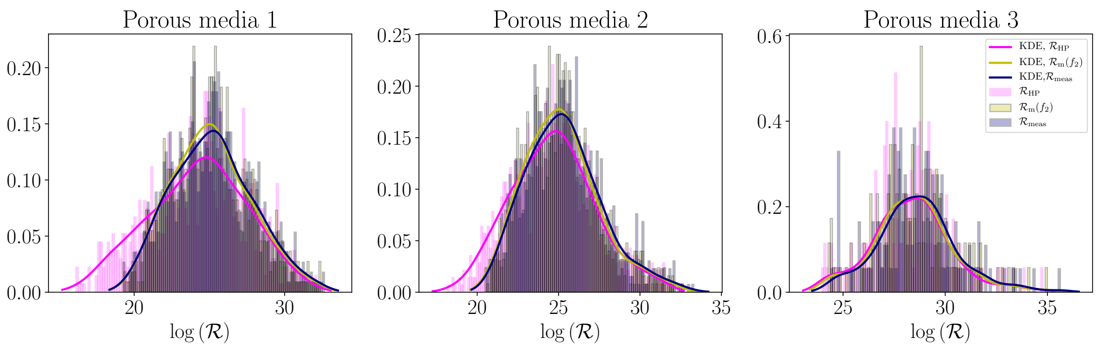

Figure S5. Histograms of the measured $\mathcal{R}_{\mathrm{meas}}$, $\mathcal{R}_{\mathrm{HP}}$ and $\mathcal{R}_{\mathrm{m}}(f_2)$.

used to build a statistical network with equivalent network topology, with each bond representing a pore with a stochastic resistance drawn from these distributions.

References

Hernderson, A. (2007). *ParaView Guide, A Parallel Visualization Application.*

Jasak, H. (1996, January). Error analysis and estimation for the finite volume method with

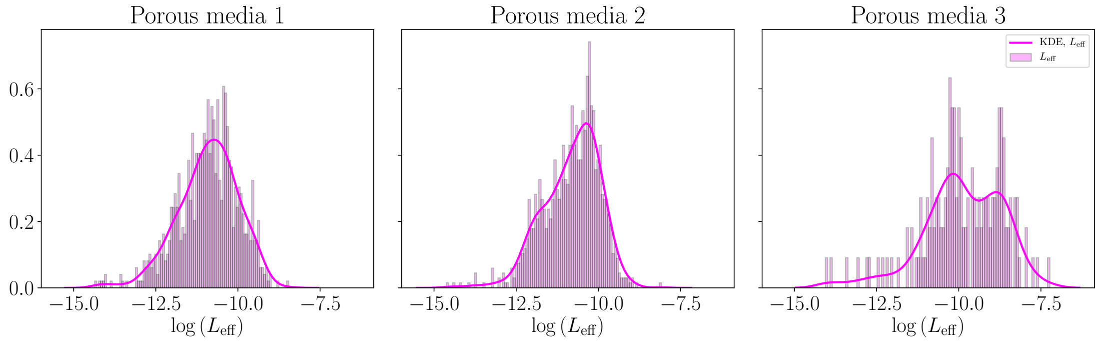

Figure S6. Histograms of the measured pore sizes L_{eff} and the KDE estimate.

applications to fluid flows.

Liu, Y., Li, J., Sun, S., & Yu, B. (2019, October). Advances in Gaussian random field generation: A review. *Comput Geosci*, *23*(5), 1011–1047. doi: 10.1007/s10596-019-09867-y

Moukalled, F., Mangani, L., & Darwish, M. (2016). *The Finite Volume Method in Computational Fluid Dynamics: An Advanced Introduction with OpenFOAM® and Matlab*. Springer International Publishing. doi: 10.1007/978-3-319-16874-6

Roberts, A., & Teubner, M. (1995, May). Transport properties of heterogeneous materials derived from Gaussian random fields: Bounds and Simulation. *Physical Review E*, *51*(5), 4141–4154. doi: 10.1103/PhysRevE.51.4141

Schroeder, W., Martin, K., & Lorensen, B. (2006). *The visualization toolkit: An object-oriented approach to 3D graphics* (4. ed ed.). Clifton Park, NY: Kitware, Inc.

Tierny, J., Favelier, G., Levine, J. A., Gueunet, C., & Michaux, M. (2018, January). The Topology ToolKit. *IEEE Transactions on Visualization and Computer Graphics*, *24*(1), 832–842. doi: 10.1109/TVCG.2017.2743938

Weller, H. G., Tabor, G., Jasak, H., & Fureby, C. (1998, December). A tensorial approach to computational continuum mechanics using object-oriented techniques. *Computers in*

Physics, *12*(6), 620. doi: 10.1063/1.168744

Wilcox, R. R. (2009, November). Comparing Pearson Correlations: Dealing with Heteroscedasticity and Nonnormality. *Communications in Statistics - Simulation and Computation*, *38*(10), 2220–2234. doi: 10.1080/03610910903289151